Nanoparticle characterization of Er-doped SnO2 pellets obtained with different pH of colloidal suspension

Leandro P. Ravaro, Luis V. A. Scalvi, Américo S. Tabata, Fenelon M. L. Pontes, and José B. B. Oliveira

Citation: Journal of Applied Physics **114**, 084304 (2013); doi: 10.1063/1.4819089
View online: http://dx.doi.org/10.1063/1.4819089
View Table of Contents: http://scitation.aip.org/content/aip/journal/jap/114/8?ver=pdfcov
Published by the AIP Publishing

Nanoparticle characterization of Er-doped SnO_2 pellets obtained with different pH of colloidal suspension

Leandro P. Ravaro,[1,2] Luis V. A. Scalvi,[1,a)] Américo S. Tabata,[1] Fenelon M. L. Pontes,[3] and José B. B. Oliveira[1]
[1]*Department of Physics—FC, UNESP—São Paulo State University, Bauru-SP, Brazil*
[2]*POSMAT, Post-Graduate Program in Materials Science and Technology, FC, Bauru-SP, Brazil*
[3]*Department of Chemistry—FC, UNESP—São Paulo State University, Bauru-SP, Brazil*

(Received 6 May 2013; accepted 6 August 2013; published online 26 August 2013)

SnO_2:2 at. %Er xerogel samples were obtained by sol-gel technique from colloidal suspensions with distinct pHs. The evaluation of critical regions inside the nanocrystallite is fundamental for the interpretation of the influence of pH on the emission data. In this way, the nanocrystal depletion layer thickness was obtained with the help of photoluminescence, Raman, X-ray diffraction, and field-emission gun scanning electron microscopy measurements. It was observed that acid suspensions ($pH < 7$) lead to high surface disorder in which a larger number of cross-linked bonds Sn-O-Sn among nanoparticles are present. For these samples, the nanoparticle depletion layer is larger as compared to samples obtained from other pH. Photoluminescence measurement in the near infrared region indicates that the emission intensity of the transition $^4I_{13/2} \rightarrow {}^4I_{15/2}$ is also influenced by the pH of the starting colloidal suspension, generating peaks more or less broadened, depending on location of Er^{3+} ions in the SnO_2 lattice (high or low symmetry sites). © *2013 AIP Publishing LLC*. [http://dx.doi.org/10.1063/1.4819089]

I. INTRODUCTION

Tin dioxide (SnO_2) is a non-stoichiometric metallic oxide (SnO_{2-x}) with n-type semiconductor characteristics, instigated by oxygen vacancies and tin interstitial atoms.[1] The SnO_2 electronic band energy diagram presents bandgap of about 3.6 eV.[2,3] Its high transparency in the visible range, mainly in the form of thin films,[4–6] has motivated wide investigation with growing interest for applications in devices based on transparent semiconductors. This oxide also presents applications in other fields such as photothermal converters for solar cells,[7] gas sensors,[8–12] opto-electronic devices,[13] among others. The transparency of SnO_2 may be combined with the emission of rare-earth ions. Among the rare-earth, Er^{3+} has high technological potential, because this ion presents a very attractive emission about 1540 nm, which coincides with the minimum absorption of silica-based optical fibers,[14,15] and belongs to the third communication window (1550 nm), used in optical fiber communication systems.[16]

It has been verified that the variation of the pH of the SnO_2 precursor solution, in the sol-gel method, leads to variation of the crystallite size and distinct oxidation rates of adsorbed gases. Increasing the solution pH yields smaller crystallites and an increase in the efficiency of the oxidation rate of CO gas,[17] due to the increase of surface area. For ZnO samples obtained from distinct precursor suspension pH, it has been also verified an unequivocal influence on both morphology and structure of obtained powders.[18,19] The effect of pH is also verified in the decrease of bandgap energy of ZnO, which gives rise to better efficiency on the energy conversion of solar cell obtained with a pH 9.[19]

In this paper, Er-doped SnO_2 samples (denoted as SnO_2:xat. %Er) were obtained from colloidal suspensions with different pH, forming SnO_2 nanoparticles with different surface defects concentrations depending on the pH. Photoluminescence (PL) spectra show a slight alteration in the emission spectra related to Er^{3+} ions located at different matrix sites, due to this colloidal suspension pH variation. The observed splitting of atomic energy levels of Er^{3+} is caused by the weak electrostatic field of the SnO_2 matrix, known as the Stark effect.[20] Then, the influence of this field on the Er^{3+} ions depends on the local symmetry. For more symmetric neighborhood, the PL emission becomes more defined and intense. The location and the local symmetry disorder of Er^{3+} populated sites are evaluated from Raman data, which justifies the less intense PL emission in samples obtained in acid-media. Field-emission gun scanning electron microscopy (FEG-SEM) data allow verifying that cross-linked bonds caused by acid pH[21] give raise to larger particles.

II. EXPERIMENTAL PROCEDURE

For the preparation of the SnO_2:Er colloidal suspension, it was used $SnCl_4.5H_2O_{(s)}$ with purity of 99.9% from Aldrich, that was transferred to a recipient along with desired amounts of $ErCl_3.3H_2O_{(s)}$ with purity of 99.9% also from Aldrich, and added distilled water, leading to a solution of concentration 0.25 ± 0.01 M. To this solution was added NH_3(aqua) (28–30 vol. %) from Ecibra until pH reaches 11, under mixing with a magnetic bar. This solution is then transferred to cellulose semipermeable bags from Sigma-Aldrich for dialysis, where most of the Cl^- and NH_4^+ ions are eliminated, resulting a neutral (pH7) stable colloidal suspension. The pH variation of colloidal suspensions was

a)Electronic mail: scalvi@fc.unesp.br

obtained by using the desired amount of NH_3(aqua) (Ecibra 28–30 vol. %) or diluted HNO_3 (Merck 65 vol. %) solution. After reaching the desired pH, the suspension remained under agitation for about 2 h. After that they were left inactive for at least 1 day, becoming ready for the xerogels preparation, which was accomplished by drying the suspension upon heating at 100 °C. The remained powders were submitted to thermal annealing (T.A.) at different times and temperatures (550 °C by 1 h, 1000 °C by 1 h, and 1000 °C by 6 h).

X-ray diffraction data were obtained with a RIGAKU diffractometer, model D/MAX-2100/PC, using Cu Kα radiation ($\lambda = 1.54$ Å), with a scanning rate of 1°/min in the range 20°–80°. The powder samples were characterized using a FEG-SEM model INSPECT F50 FEI.

For the PL measurements in the infrared range, samples were excited with the 488 nm line of an Argon (Ar^+) laser and the signal was detected by a germanium detector cooled with liquid nitrogen. In the PL measurements, the sample temperature was controlled by using a closed cycle He cryostat. A single configuration monochromator was used for selecting the emitted signal. Raman spectroscopy was carried out in a triple spectrophotometer Jobin-Yvon model T64000 in subtractive configuration with a CCD detector, also cooled with liquid nitrogen. The same line of the Ar^+ laser (488 nm) was used as light source.

III. RESULTS AND DISCUSSION

Figure 1 shows Raman spectra evolution for SnO_2:2at. %Er pellets (compressed powder with 5000 kgf/cm^2 on a rectangular pattern) for different thermal annealing conditions (time and temperature). Figure 1(a) shows the sample thermally annealed at 550 °C by 1 h. For all samples, only the vibration mode A_{1g} is clearly observed. Increasing the thermal annealing temperature (and time) for 1000 °C by 6 h (Fig. 1(b)), the vibration mode B_{2g} also becomes evident for all the samples. For the pH 4 sample, it is possible to identify other modes (S_2, A_{1g}, S_3, B_{2g}). The modes A_{1g} and B_{2g} nondegenerate are related to oxygen atoms vibrating in a plane perpendicular to the c axis on the SnO_2 unit cell. The vibration modes B_{1g} and E_g (not seen in the spectra of Figure 1) are hard to be found due to their low intensity when compared to other vibration modes.[22] For instance, the intensity of mode B_{1g} is about 10^{-3} of A_{1g}. Other vibration modes for SnO_2 can be found in a more complete analysis, published elsewhere.[23] The goal in this paper is to evaluate the crystallite depletion layer, using the most intense peaks of Figure 1, related do the modes A_{1g}, S_1, and S_2.

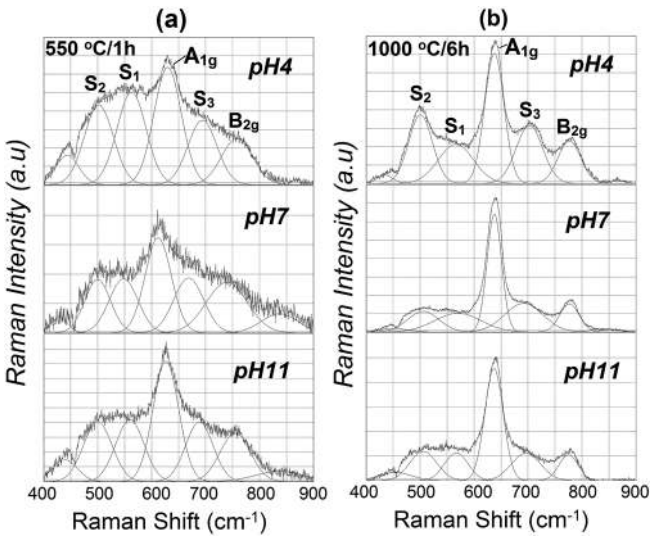

FIG. 1. Raman spectra evolution for different conditions (time and temperature) of thermal annealing (T.A.) for SnO_2:2 at. %Er samples, obtained from colloidal suspension with different pH. Band deconvolution curves are also shown. (a): T.A. 550 °C/1 h. (b): T.A. 1000 °C/6 h.

The vibration S_1, S_2, and S_3 are related to the acoustic modes, which indicate a break of large order symmetry and materials imperfections.[22,24] Then, based on Fig. 1, the pH 4 sample would have more imperfections and symmetry break as compared to pH 7 and pH 11 pellets, because vibrations S_2 and S_3 are more intense in the pH 4 sample. This symmetry break may be caused by coalescence of nanoparticles in the colloidal suspension due to cross-linked bounds (Sn-O-Sn),[21] which takes place as the colloidal suspension pH becomes more acid. Then, linked nanoparticles give rise to larger agglomerates and, then, to larges grains, with higher amount of imperfections and oxygen vacancies. In the case of Sb-doped SnO_2, it was found that the oxygen vacancies surround the substitutional Sb ions, located at grain boundary.[25] We believe that it may be similar to Er-doped SnO_2. Table I shows a comparison between published vibration modes and the values found here.

Figure 2 is a schematic diagram, showing defects generated after coalescence between nanoparticles in the acid colloidal suspension. In acid media, the colloidal particles of SnO_2 tend to form larger agglomerates due to electrostatic attraction between them. This is correct as long as the pH is not below the isoelectric point, which is given in the literature as in the range 3.5–4.[28–30] For acid pH, above this isoelectric point, as the particles get closer to each other, the probability of Sn-O-Sn cross-linked bonds formation proportionally increases. For the case of pH 4, we believe that the attraction between particles is still the rule, even though with the proximity of the isoelectric point the repulsion between some of them may start to take place. This sort of larger agglomerates formed, due to attraction between particles, is rich in punctual defects such as oxygen vacancies, mainly at grain boundary (depletion layer). Besides, three-dimensional defects such as pores may also be present. These possibilities are illustrated in Figure 2.

TABLE I. Values of some vibration modes for the SnO_2 tetragonal structure.

Vibration modes (references)	A_{1g} (cm^{-1})	B_{2g} (cm^{-1})	S_1 (cm^{-1})	S_2 (cm^{-1})	S_3 (cm^{-1})
26	638	782	—	—	—
27	634	776	—	—	—
22	634	776	568	486	706
24	640	780	—	510	700
Exp., Fig. 1(b), pH 4	640 ± 0.5	782 ± 0.5	565 ± 0.2	499 ± 1	702 ± 0.2

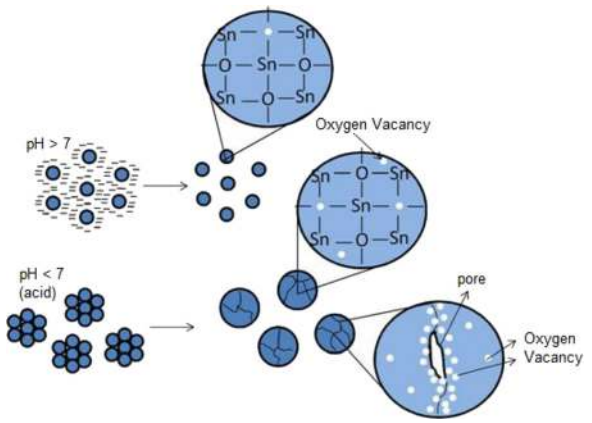

FIG. 2. Diagram showing the interaction between colloidal nanoparticles in basic or acid media, along with generation of punctual defects (vacancies) and three-dimensional defects (pores).

The position of vibration modes found for SnO_2:2 at. %Er are in good agreement with the literature (Table I). However, it is possible to observe that there is a variation in the Raman spectra for the different pH samples. This is an indication that the colloidal suspension pH may be leading to an alteration on the disordered layer, which means on the depletion layer. The SnO_2 nanoparticle presents two distinct regions: a higher symmetry bulk and a highly disordered periphery, which constitute the grain boundary depletion layer. In a disordered material, imperfections modify its local symmetry, avoiding the in-phase vibration of neighbor atoms, due to the break of long range order. This reduces the contribution of optically active phonons to the Raman spectra. As the S_1, S_2, and S_3 modes are originated in this region this becomes more evident as the layer thickness increases. Then, the results shown in Figure 1 suggest that this disordered region increases with the pH decrease.

Fig. 3 shows schematically the Raman bands and the relation with the high symmetry bulk and the disordered region (depletion layer), inside the SnO_2 nanoparticle.

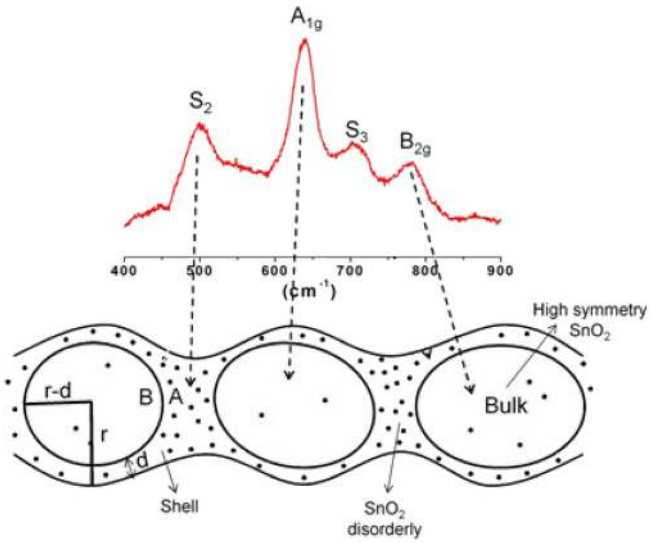

FIG. 3. Raman spectra of SnO_2:2 at. %Er powder sample with pH 4, where the bottom illustration indicates the high and low symmetry regions of the nanoparticles.

Dieguez and coworkers[22] proposed a calculation method to evaluate the thickness of the depletion layer and the bulk from the Raman spectra. It can be summarized as the division of bands related to imperfection (surface) area by the one related to the bulk. This ratio would be directly proportional to the volume of the depletion layer and the bulk one ($A_{surface\ modes}/A_{bulk\ modes} \propto V_{shell}/V_{bulk}$). Then, it yields an estimative of the depletion layer, considering that the crystallite average size is known. This calculation was carried out for our samples. Assuming that each nanocrystal is approximately spherical with radius r and composed of a crystalline nucleus of radius (r-d), surrounded by an external cap, which is the disordered layer with thickness d, the ratio of corresponding volumes is directly related to the corresponding areas of bands in the Raman spectra, and can be expressed by Eq. (1), where $A_{surface\ modes} = A_{S1+S2}$ and $A_{bulk\ modes} = A_{A1g}$. Then,[22]

$$\frac{A_{S1+S2}}{A_{1g}} \alpha \frac{V_{shell}}{V_{bulk}} = \left[\left(\frac{r}{r-d}\right)^3 - 1\right], \quad (1)$$

where A_{S1+S2} is the sum of the areas under the bands S_1 and S_2 of the Raman spectra, A_{A1g} is the area under the band A_{1g} of the Raman spectra. V_{shell} and V_{bulk} are the volumes of the disordered layer and the bulk of the nanocrystal, respectively.

Figure 4 shows X-rays diffractograms for SnO_2:2 at. %Er powder obtained from different pH samples, submitted to thermal annealing of 550 °C/1 h (left side figures) and 1000 °C/6 h (right side figures). Table II presents the values of the average crystallite size (evaluated through the Scherrer equation[31]), for samples SnO_2:2 at. %Er with pHs 4, 7, and 11. Table II also brings the estimative of bulk and depletion layer thickness as proposed by Eq. (1), and the relative shell volume is compared to the total crystallite volume. As can be seen, the same annealing condition leads to very close crystallite sizes. Samples with T.A. of 550 °C/1 h present average crystallite size with diameter 4.9 nm, 5.3 nm, and 4.8 ± 0.1 nm for pH 4, 7, and 11, respectively, whereas

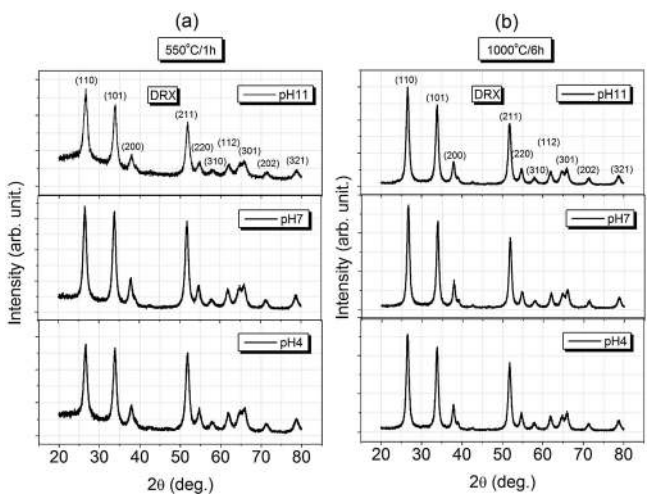

FIG. 4. X-ray diffractograms of SnO_2:2 at. %Er powders obtained from colloidal suspensions with pHs 4, 7, and 11. (a): T.A. 550 °C/1 h. (b): T.A. 1000 °C/6 h.

TABLE II. Average size (t), disordered layer thickness (d) and relative volume (v_{shell}/v_{total}) % of disordered shell for SnO_2:2 at. %Er nanocrystal from samples obtained from different pHs.

	550 °C/1 h			1000 °C/6 h		
Sample	t (nm)	d (nm)	(v_{shell}/v_{total}) %	t (nm)	d (nm)	(v_{shell}/v_{total}) %
pH 4	4.9	0.67	62	10.7	1.23	53
pH 7	5.3	0.60	54	11.0	1.00	40
pH 11	4.8	0.50	50	10.0	0.80	36

T.A. of 1000 °C/6 h leads to diameter of 10.7 nm, 11.0 nm, and 10.0 ± 0.1 nm for pH 4, 7, and 11, respectively. As can be seen, thermal annealing temperature practically determines the crystallite diameter, which is to double up from 550 °C to 1000 °C, but no significant variation is observed due to pH variation for the samples submitted to the same thermal annealing.

Considering that the ratio obtained by dividing the area of the Raman bands ($S_1 + S_2$) by the area of the band (A_{1g}) is proportional to ratio between the volume of Shell and bulk volume (V_{shell}/V_{bulk}),[22] as predicted by Eq. (1), it is possible to estimate the thickness of the disordered layer (d) of the SnO_2 nanocrystallites obtained with different pHs. The area under the corresponding Raman band is evaluated from the Gaussian deconvolution of the Raman spectra. Taking into account the crystallite size evaluated from the X-ray diffractograms of Fig. 4, this ratio was calculated and it is also presented in Table II. Fig. 5 shows this ratio as function of the precursor colloidal suspension pH.

It is possible to verify from Fig. 5 and Table II that as the pH decreases, there is a larger contribution from areas A_{S1+S2} as compared to the area A_{A1g}. This is an indication that nanoparticles generated from acid suspensions show a thicker imperfection region compared to nanoparticles obtained from more basic suspensions. It is also possible to observe that the relative V_{shell}/V_{bulk} decreases as the thermal annealing temperature increases (curve b of Fig. 5). In fact, the magnitude of the depletion layer increases with the annealing temperature, but the relative volume of the disordered shell decreases, indicating a lower disordered fraction. The evaluated shell volume compared to the nanocrystallite volume (V_{shell}/V_{total})% for SnO_2:2 at. %Er with T.A. of 550 °C/1 h were 62%, 54%, and 50%, for samples obtained from pHs 4, 7, and 11, respectively. When the T.A. temperature and time are raised (1000 °C by 6 h), the found ratios were 53%, 40%, and 36%, respectively.

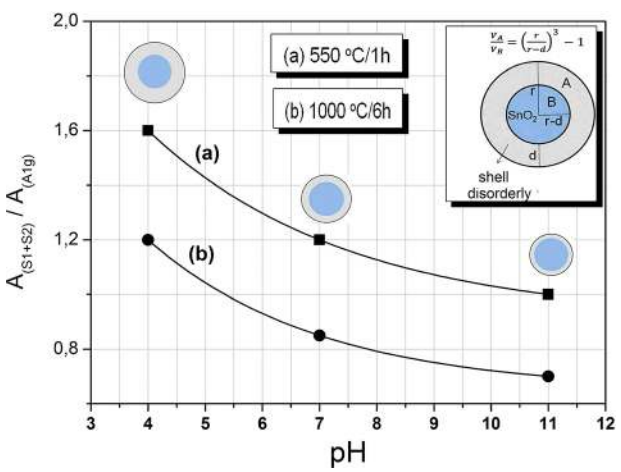

FIG. 5. Ratio between the sum of areas of bands S_1 and S_2 and area of band A_{1g} as function of pH (lines are drawn as a guide, because only three pH values are plotted).

Fig. 6 shows FEG-SEM images for SnO_2:2 at. %Er powder samples treated at 1000 °C/6 h. It is possible to observe the porosity for each sample, obtained with distinct pH. It is also possible to verify the grain dimensions, which grows as the pH of the colloidal suspension decreases. The evaluated average grain size was 28 nm, 21 nm, and 19 nm for samples obtained from pH 4, 7, and 11, respectively. These results confirm that acid suspensions lead to the formation of larger grains, which are induced by means of cross-linked bonds[21] between SnO_2 nanoparticles. On the other hand, the grains of sample obtained from pH 4 (Figs. 6(a) and 6(b)) present a more elliptical shape than pH 7 sample (Figs. 6(c) and 6(d)), which are relatively more elliptical-shaped than grains of pH 11 sample (Figs. 6(e) and 6(f)). The nanometric dimensions of grains obtained by the FEG-SEM results are a little bit higher than the dimensions obtained from the Scherrer equation (Table II), which has shown that a particle may be made up of several different crystallites.

Figure 7 shows FEG-SEM images for 1 at. %-doped SnO_2 powder samples also obtained from colloidal suspension with distinct pH, thermally annealed at 550 °C/1 h. It is possible to verify that the pH 4 powder (Fig. 7(a)) is composed of agglomerates in the form of squared blocks and uneven aspect, whereas the powder obtained from colloidal suspension with pH 11 show chips format with smooth aspect (Fig. 7(c)). The average grain size for SnO_2:1 at. %Er samples decreases with pH, being 22 nm, 13 nm, and 11 ± 0.1 nm for samples obtained from pHs 4, 7, and 11, respectively. A comparison of grain size between samples with different Er concentration is not possible, because samples of Figures 6 and 7 are treated at rather distinct annealing conditions. On the other hand, the crystallite size, evaluated through the Scherrer equation for 1at. %-doped SnO_2 powder samples, yields 6.5 nm, 6.4 nm, and 6.3 ± 0.1 nm for pH 4, 7, and 11, respectively. These values are larger than the values for 2 at. %-doped SnO_2 shown at Table II, suggesting that the larger Er concentration leads to smaller crystallites.

Figure 8 shows PL results for 2 at. % Er-doped xerogels, obtained from colloidal suspension with altered pH from the neutral pH. Monochromatic excitation is accomplished by the 488 nm line of an Ar^+ laser, with 100 mW of power. These measurements were taken at low temperature (T = 9 K). Figure 8(a) shows PL spectra for samples annealed at 1000 °C for 1 h. It is possible to observe the peaks related to the radiative transition of excited state $^4I_{13/2}$ to the ground state $^4I_{15/2}$ for all the analyzed samples. The emission fine structure is slightly dependent on the pH. For the SnO_2:2 at. %Er submitted to a longer annealing (1000 °C/6 h, Figure 8(b)), the emission is better defined. Figure 8(b) allows observing that the emission spectra obtained from the pH 7 sample is more intense than the one

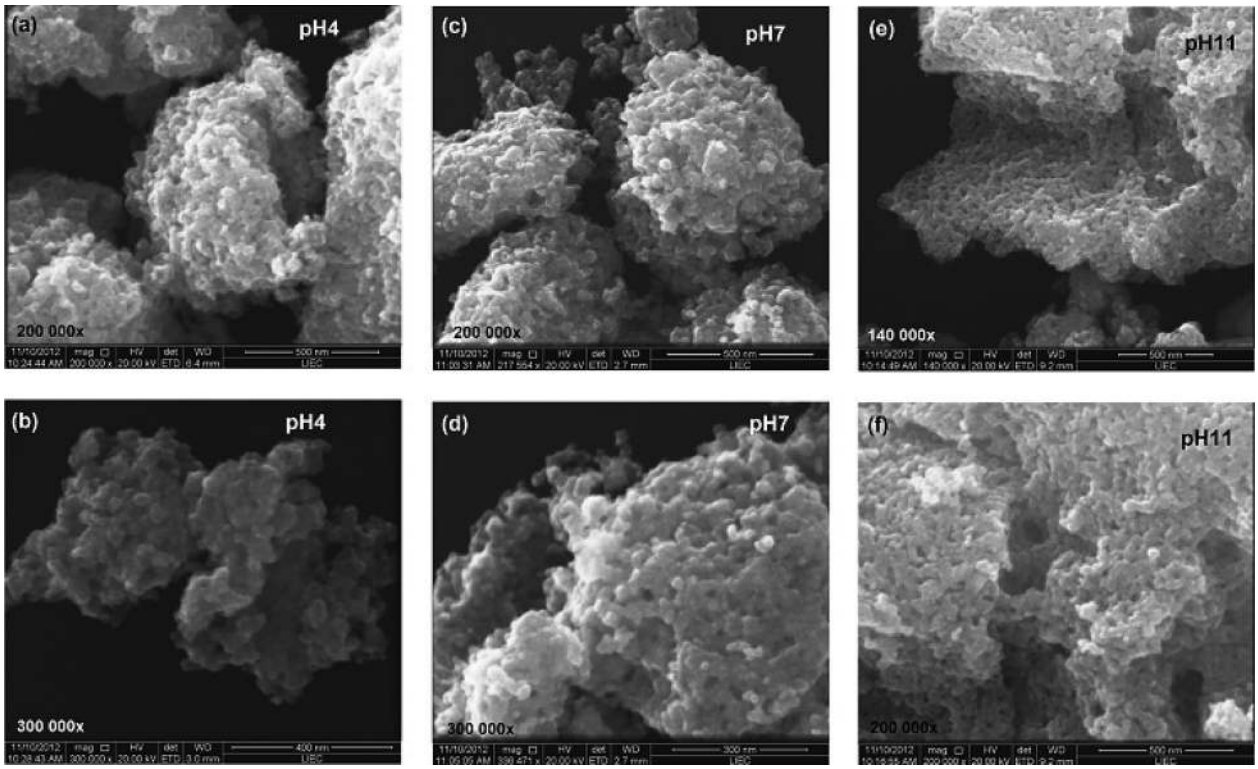

FIG. 6. FEG–SEM images for SnO_2:2 at. %Er samples obtained from colloidal suspensions with distinct pH (4, 7, and 11) and T.A. of 1000 °C/6 h.

obtained from the pH 4 sample, which in turn is more intense than the pH 11 sample. Emission peaks are observed at 1513 nm, 1518 nm, 1522 nm, 1524 nm, 1530 nm, 1532 nm, 1535 nm, 1542 nm, 1546 nm, 1550 nm, 1568 nm, and 1572 nm for samples obtained from pH 4 and 7. For the pH 11 sample, most of these peaks in the PL spectra are not well defined. The first and the second most intense peaks happens at 1530 nm and 1533 nm, respectively, for the PL spectra

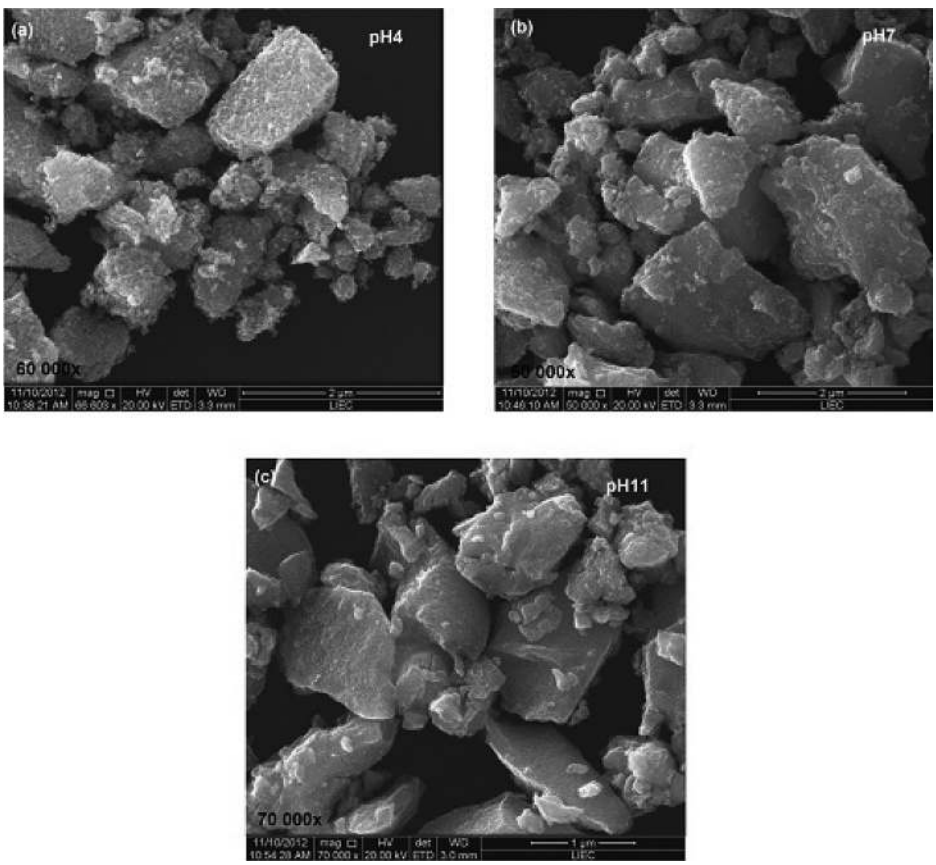

FIG. 7. FEG–SEM images for SnO_2:1 at. %Er samples obtained from colloidal suspensions with distinct pH (4, 7, and 11) and T.A. of 550 °C/1 h.

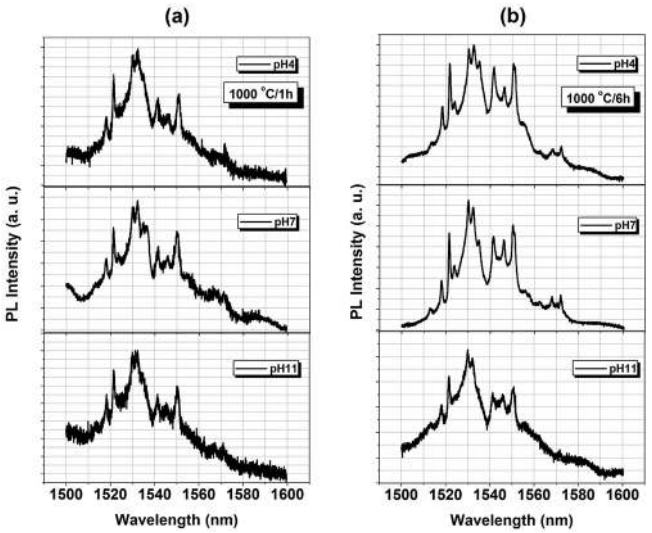

FIG. 8. Evolution of PL spectra as function of T.A. for SnO_2:2 at. %Er pellets obtained from pH 4, 7, and 11. (a): T.A. 1000 °C/1 h and (b): T.A. 1000 °C/6 h. Excitation source: 488 nm Ar^+ laser line.

from pH 11 and pH 7 samples, whereas for the pH 4 a inversion between these intensities takes place, and the most intense peak is the 1533 nm.

This inversion in the most intense peak for the pH 4 sample may be related to the type of site occupied by the Er^{3+} ions in the SnO_2 nanocrystals, which are more disordered with distinct defects concentration surrounding it, as inferred from the Raman results already presented. It would explain the exchange in the intensities and the broader spectra for the pH 4 sample in the range between 1530 nm and 1533 nm. A schematic diagram based on this assumption is shown in Figure 9. Eu^{3+} (europium) has solubility-limit about 0.05 at. % in the SnO_2 matrix.[32,33] This low solubility is related, mainly, to the difference between ionic radius of Eu^{3+} (0.95 Å) and Sn^{+4} (0.76 Å).[34] On the other hand, Er^{3+} has ionic radius of 0.89 Å,[35] and then, it is believed that Er^{3+}

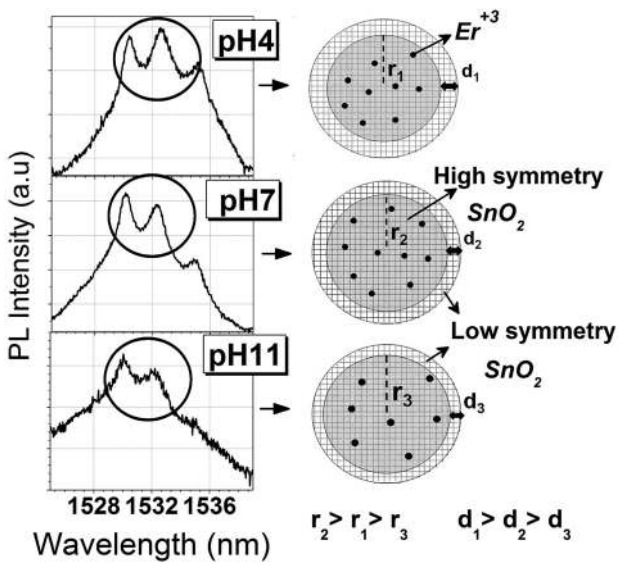

FIG. 9. Configuration of emission peak about 1532 nm as function of external and internal symmetry of the nanocrystallite for SnO_2:Er2% pellets with distinct pHs.

presents similar solubility (0.05 at. %) in the SnO_2 matrix, where the excess segregates to the grain boundary layer. The investigated samples present 2 at. % of Er^{3+}, which means that about 1.95% of this dopant must be located in the disordered region of SnO_2 matrix, at the grain boundary layer. However, the Er^{3+} emission is better defined and more intense for the samples with larger crystallites.

Although the grain size is a little bit larger for the pH 4 sample, the crystallite size is about the same for all the samples, which means that the amount of crystallites inside the grain is higher for the pH 4 sample (due to coalescence by cross-linked bonds) as compared to the pH 7 sample or pH 11. Actually, the sample obtained from neutral pH presents slightly larger crystallites, besides, the pH 4 sample presents thicker disordered region (Table II), which could explain the less intense emission of the acid sample compared to the obtained sample from neutral pH, since the Er^{3+} emission is more intense for higher symmetry located ions. Although the Er^{3+} concentration is lower in the bulk compared to the surface concentration, the higher PL signal in the neutral sample shows that the PL signal carries qualitative information concerning the Er^{3+} ion distribution, located in the bulk and in the boundary layer.

Concerning the several peaks observed in the PL spectra, they are related to the electronic transition between the levels $^4I_{13/2}$ and $^4I_{15/2}$. There is a splitting of these two levels ^4I_J in $J + 1/2$ new defined levels, due to influence of the weak electric field on the optically active electrons (4f) of Er^{3+} ions (Stark effect).[20] Then, between the levels $^4I_{13/2}$ and $^4I_{15/2}$ there are several fine and well-defined levels, associated to the observed emission spectra. Some Stark peaks present an inhomogeneous splitting due to electric field variation in different sites occupied by the Er^{3+} ion in the SnO_2 nanocrystal.[36,37] When the Er^{3+} neighborhood changes, the electric field also changes due to the random neighbor distribution, characteristic of materials with nanoscopic crystallites, generating small variations in the positions of the Stark levels.

Figure 10 presents some details concerning the PL spectra acquired at 9 K, related to Er^{3+} transitions of SnO_2:Er 2

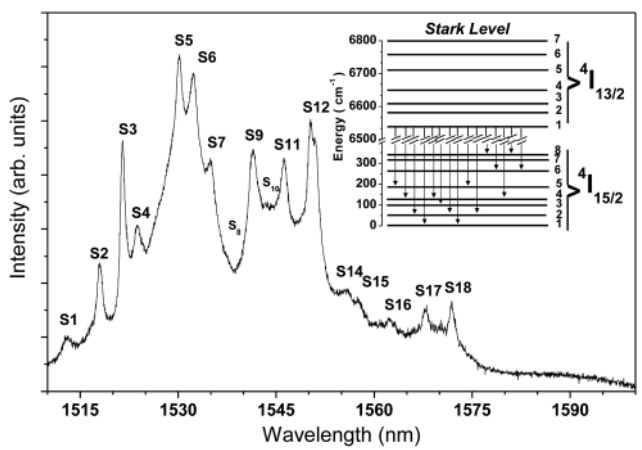

FIG. 10. Infrared emission spectra for SnO_2:Er2 at. % obtained from pH 7, at 9 K, exhibiting the Stark levels. Excitation source: 488 nm Ar^+ laser line. Inset: diagram showing the Stark components between the levels $^4I_{13/2}$ and $^4I_{15/2}$ for the observed peaks.

TABLE III. Detailed infrared transitions for SnO_2:Er2 at. % with pH 7.

Stark component	$^4I_{13/2} \rightarrow {}^4I_{15/2}$ (nm)	Peak	Stark component	$^4I_{13/2} \rightarrow {}^4I_{15/2}$ (nm)	Peak
1-1	1512.6	S1	1-2	1543.4	S10
1-2	1518.0	S2	1-5	1546.2	S11
1-4	1521.5	S3	1-3	1550.3	S12
1-2	1523.7	S4	1-6	1551.0	S13
1-6	1530.1	S5	1-4	1555.0	S14
1-1	1532.2	S6	1-8	1557.4	S15
1-2	1534.8	S7	1-4	1562.2	S16
1-3	1541.4	S8	1-8	1568.0	S17
1-6	1541.4	S9	1-5	1571.8	S18

at. % powder obtained with pH 7, submitted to thermal annealing at 1000 °C for 6 h. The inset of Figure 10 illustrates the observed Stark peaks between the $^4I_{13/2}$ and $^4I_{15/2}$. These Stark peaks shown in Figure 10 are listed in Table III. The effect of the different pH of the starting solution on the Stark levels can be verified through the broadening of the peak width. Table IV shows the full width at half maximum of some peaks, obtained from Gaussian deconvolution of the PL spectra. Generally speaking, the comparison between different pH shows that most of the peaks present a broadening for pH variation compared to the pH 7 sample, being more evident for pH 11 (basic media). This broadening is due to the overlapping of Stark peaks originated from the transition $^4I_{13/2} \rightarrow {}^4I_{15/2}$,[20,38] which becomes broader as the disorder increases. They may present an inhomogeneous broadening due to electric field variation at different sites,[37,39] which changes from site to site due to the random distribution of neighbors, characteristic of nanoscopic crystallites, mainly considering that the solubility limit has been overcome.

IV. CONCLUSIONS

The pH variation of precursor solution leads to some alterations on the physical properties of Er-doped tin dioxide. X-ray diffraction, Raman spectroscopy, and FEG-SEM results point to the formation of larger grains and higher concentration of grain boundary defects for samples prepared from acid solutions. Photoluminescence data reveal that the PL emission intensity has a close relation with the bulk size of SnO_2 nanocrystallite and the concentration of surface layer defects. The PL emission increases when the nanocrystallite bulk size increases whereas the surface defects decrease. Also, it was observed that the Er^{3+} ions located at surface layer present PL emission less intense and broader due to the random neighborhood distribution and interaction among doping ions, which are closer to each other in this case. The higher amount of cross-linked bonds between colloidal particles for acid pHs gives rise to more disordered sites for Er^{3+} in the depletion layer of SnO_2 grains, which slightly shift the Stark components in the emission spectra.

We must reinforce that the present investigation aims to contribute for a better understanding of luminescent properties of Er-doped SnO_2, mainly concerning its control through physical-chemistry properties of the sol-gel route. The procedure presented here allows preparing materials composed of nanoparticles, and suggests ways of controlling the physical location of the doping ions inside the nanoparticles. These are good contributions to avoid low quantum efficiency in rare-earth doped SnO_2 devices.

TABLE IV. Full width at half maximum (W) of selected peaks for samples SnO_2:Er2% with distinct pH.

Peak	pH 7 W (nm)	pH 4 W (nm)	pH 11 W (nm)
S3	0.64	0.71	0.85
S4	3.56	2.93	7.82
S5	4.30	4.32	3.66
S6	0.82	0.82	0.97
S7	3.50	3.79	4.67
S8	2.33	1.99	1.91
S9	3.93	4.74	5.08
S10	1.97	1.70	1.92

ACKNOWLEDGMENTS

The authors also thank the Brazilian financial agencies: CAPES, CNPq, and FAPESP.

[1]C. Xu, Y. Jiang, D. Yi, S. Sun, and Z. Yu, J. Appl. Phys. **111**, 063504 (2012).
[2]J. Rockenberger, U. Z. Felde, M. Tischer, L. Tröger, M. Haase, and H. Weller, J. Chem. Phys. **112**, 4296 (2000).
[3]Y. Li, R. Deng, Y. Tian, B. Yao, and T. Wu, Appl. Phys. Lett. **100**, 172402 (2012).
[4]I. Maksimenko and P. J. Wellmann, Thin Solid Films **520**, 1341 (2011).
[5]Y. J. Shin, Q. Zhang, and F. Hua, Thin Solid Films **516**, 3167 (2008).
[6]J. Robertson, J. Non-Cryst. Solids **354**, 2791 (2008).
[7]E. O. Igbinovia and P. A. Llenikhena, Int. J. Phys. Sci. **5**, 1770 (2010).
[8]S. F. Bamsaouda, S. B. Rane, R. N. Karekar, and R. C. Ayier, Sens. Actuators B **153**, 382 (2011).
[9]A. Heilig, N. Barsan, U. Weimar, and W. Göspel, Sens. Actuators B **58**, 302 (1999).
[10]S. G. Ansari, Z. A. Ansari, R. Wahab, Y. S. Kim, G. Khang, and H. S. Shin, Biosens. Bioelectron. **23**, 1838 (2008).
[11]J. Sun, J. Xu, Y. Yu, P. Sun, F. Liu, and G. Lu, Sens. Actuators B **169**, 291 (2012).
[12]B. Adamowicz, W. Izydorczyk, J. Izydorczyk, A. Klimasek, W. Jakubik, and J. Żywicki, Vacuum **82**, 966 (2008).
[13]C. Terrier, J. P. Chatelon, and J. A. Roger, Thin Solid Films **295**, 95 (1997).
[14]S. Coffa, G. Franzó, F. Priolo, A. Polman, and R. Serna, Phys. Rev. B **49**, 16313 (1994).
[15]J. Castaneda-Contreras, M. A. Meneses-Nava, O. Barbosa-Garcia, R. A. Rodriguez-Rojas, and M. V. Félix, Opt. Mater. **29**, 38 (2006).
[16]A. J. Kenyon, Prog. Quantum Electron. **26**, 225 (2002).
[17]F. Lan, X. Wang, X. Xu, R. Zhang, and N. Zhang, React. Kinet. Mech. Catal. **106**, 113 (2012).
[18]A. Al-Kahlout, Thin Solid Films **520**, 1814 (2012).
[19]S. Rani, P. Suri, P. K. Shishodia, and R. M. Mehra, Sol. Energy Mater. Sol. Cells **92**, 1639 (2008).
[20]R. Maâlej, M. Dammak, S. Kammoun, and M. Kammoun, J. Lumin. **126**, 695 (2007).
[21]R. S. Hiratsuka, C. V. Santilli, D. V. Silva, and S. H. Pulcinelli, J. Non-Cryst. Solids **147–148**, 67 (1992).
[22]A. Dieguez, A. Romano-Rodrıguez, A. Vila, and J. R. Morante, J. Appl. Phys. **90**, 1550 (2001).
[23]L. P. Ravaro, A. Tabata, J. B. B. Oliveira, and L. V. A. Scalvi, Opt. Mater. **33**, 66 (2010).
[24]E. A. Morais, L. V. A. Scalvi, A. A. Cavalheiro, A. Tabata, and J. B. B. Oliveira, J. Non-Cryst. Solids **354**, 4840 (2008).

[25]V. Geraldo, V. Briois, L. V. A. Scalvi, and C. V. Santilli, J. Eur. Ceram. Soc. **27**, 4265 (2007).
[26]R. S. Katiyar, J. Phys. C: Solid State Phys. **3**, 1087 (1970).
[27]P. S. Peercy and B. Morosin, Phys. Rev. B **7**, 2779 (1973).
[28]V. Rodriguez-Santiago, M. V. Fedkin, D. J. Wesolowski, J. Rosenqvist, and S. N. Lvov, Langmuir **25**, 8101 (2009).
[29]S. Belin, L. R. B. Santos, V. Briois, A. Lusvardi, C. V. Santilli, S. H. Pulcinelli, T. Chartier, and A. Larbot, Colloids Surf., A **216**, 195 (2003).
[30]M. C. Esteves, D. Gouvea, and P. T. A. Sumodjo, Appl. Surf. Sci. **229**, 24 (2004).
[31]B. D. Cullity and R. Stock, *Elements of X-Ray Diffraction* (Prentice Hall, New Jersey, 2001).
[32]D. Lahiri, R. S. Ningthoujam, D. Bhattacharyya, and S. M. Sharma, J. Appl. Phys. **107**, 054316 (2010).
[33]A. C. Yanes, J. Del Castillo, M. Torres, J. Peraza, V. D. Rodríguez, and J. Méndez-Ramos, Appl. Phys. Lett. **85**, 2343 (2004).
[34]R. S. Ningthoujam, V. Sudarsan, and S. K. Kulshreshtha, J. Lumin. **127**, 747 (2007).
[35]T. T. Van, J. Hoang, R. Ostroumov, K. L. Wang, J. R. Bargar, J. Lu, H.-O. Blom, and J. P. Chang, J. Appl. Phys. **100**, 073512 (2006).
[36]L. R. Tessler and A. C. Iñiguez, J. Non-Cryst. Solids **266–269**, 603 (2000).
[37]E. A. Morais, S. J. L. Ribeiro, L. V. A. Scalvi, C. V. Santilli, L. O. Ruggiero, S. H. Pulcinelli, and Y. Messaddeq, J. Alloys Compd. **344**, 217 (2002).
[38]F. Auzel, J. Non-Cryst. Solids **354**, 4765 (2008).
[39]L. J. Q. Maia, C. R. Ferrari, V. R. Mastelaro, A. C. Hermandez, and A. Ibanez, Solid State Sci. **10**, 1835 (2008).